Nano Energy 89 (2021) 106480

Contents lists available at ScienceDirect

Nano Energy

journal homepage: www.elsevier.com/locate/nanoen

Full paper

A newly-explored Pd-based nanocrystal for the pH-universal electrosynthesis of H_2O_2

Chengyong Yang [a,1], Shuxing Bai [a,1], Zhiyong Yu [a], Yonggang Feng [a], Bolong Huang [b,*], Qiuyang Lu [b], Tong Wu [b], Mingzi Sun [b], Ting Zhu [a], Chen Cheng [c], Liang Zhang [c], Qi Shao [a], Xiaoqing Huang [a,d,**]

[a] College of Chemistry, Chemical Engineering and Materials Science, Soochow University, Jiangsu 215123, China
[b] Department of Applied Biology and Chemical Technology, The Hong Kong Polytechnic University, Hung Hom, Kowloon, Hong Kong SAR 999077, China
[c] Institute of Functional Nano & Soft Materials (FUNSOM), Jiangsu Key Laboratory for Carbon-Based Functional Materials and Devices, Soochow University, Jiangsu 215123, China
[d] College of Chemistry and Chemical Engineering, Xiamen University, Xiamen 361005, China

ARTICLE INFO

Keywords:
SePd alloy
PH-universal
H_2O_2 electrosynthesis
High selectivity
P-d coupling

ABSTRACT

For the generation of hydrogen peroxide (H_2O_2), a robust electrocatalyst with high activity, selectivity and stability under pH-universal conditions is a formidable challenge. Herein, Pd_4Se nanoparticles (NPs) have been proposed as a highly active, selective and durable electrocatalyst for H_2O_2 production over a wide pH range for the first time. In particular, the Pd_4Se NPs show superior H_2O_2 production selectivities of 93.5%, 89.7%, and 86.7% in 0.1 M $HClO_4$, 0.1 M KCl and 0.1 M KOH electrolytes, respectively. Density functional theory (DFT) calculations reveal that Se incorporation prevents the O═O early-cleavage issue by suppressing the excessive electronegativity of the Pd sites. In addition, a strong p-d repulsive correlation shifts the Pd-4d band towards the electron-depleting centre, allowing near-barrier-free electron transfer and facilitating [OOH^-] stabilization. Owing to a high energy barrier of the dissociation of [OOH^-], the four-electrons oxygen reduction pathway is significantly suppressed for high H_2O_2 selectivity. The Pd_4Se NPs are also highly stable, with only a 2.4%, 9.6% and 3.4% decrease for H_2O_2 selectivity in 0.1 M $HClO_4$, 0.1 M KCl and 0.1 M KOH electrolytes, respectively, after 5000 cycles, which shows that these NPs are a unique and robust Pd-based electrocatalyst for H_2O_2 generation under pH-universal conditions.

1. Introduction

Hydrogen peroxide (H_2O_2) is a multifunctional and environmentally friendly oxidant, which has been extensively applied in industry, medicine, environmental protection, etc. [1–5] At present, the industrial production of H_2O_2 is via the hydrogenation by H_2 and subsequent oxidation with O_2 using anthraquinone as substrate in the organic solvent system. [6,7] As the state-of-the-art large-scale production technology, this process still needs to face serious sustainability challenges, such as safety issues, the costs of transportation and storage due to the instability of H_2O_2, the use of large amounts of organic solvents and the handling of industrial wastes. The direct synthesis of H_2O_2 starting from H_2 and O_2 with the existence of catalysts offers a more efficient route, which ideally resolves many of the deficiencies related to the indirect anthraquinone process. [8,9] Nevertheless, due to the potential explosive hazard from the mixture of H_2 and O_2, safety concerns also hinder their practical applications. Therefore, it is still of great desire to develop a more direct, efficient, and economical H_2O_2 production method. [10,11].

Recently, an electrochemical strategy using oxygen reduction has gained substantial interest because it effectively addresses the issues related to both the indirect anthraquinone method and direct synthetic processes. [12–14] Regarding the oxygen reduction reaction (ORR), the studies are mainly focused on finding an ideal catalyst for the selective reduction of O_2 to H_2O_2 through a $2e^-$ reduction pathway from both experimental and theoretical investigations. [15–22,48,49] Recently,

* Corresponding author.
** Corresponding author at: College of Chemistry, Chemical Engineering and Materials Science, Soochow University, Jiangsu 215123, China.
E-mail addresses: bhuang@polyu.edu.hk (B. Huang), hxq006@suda.edu.cn (X. Huang).
[1] Chengyong Yang and Shuxing Bai contributed equally to this work.

https://doi.org/10.1016/j.nanoen.2021.106480

Available online 30 August 2021

noble metals and their alloys (Pt-Hg, [23] Pd-Au, [24] and Pd-Hg [25]) have been readily used as catalysts for the production of H_2O_2. For example, Rossmeisl's group has screened out new alloy electrocatalysts through DFT calculations and obtained the best *OOH (adsorbed intermediate for H_2O_2 production) binding values by isolating the active site in reactive metals (i.e., Pt and Pd) with inactive Hg and, finally, high selectivity towards H_2O_2 production is achieved in 0.1 M $HClO_4$. [23] Amal's group have successfully established Au-Ni and Au-Pt-Ni core--shell nanorods electrocatalysts by using Au nanorods with high-index facets as the substrate, which showed relatively high performance toward the synthesis of H_2O_2 in 0.1 M KOH. [26] Carbon-based materials are another class of catalysts that have been intensively studied for H_2O_2 electrosynthesis, this kind of electrocatalyst typically possesses a relatively high specific surface area, efficient mass transfer properties, and special active sites for oxygen activation. [27] However, the further application of the carbon-based catalysts is hindered by the low efficiency as well as poor stability under harsh environments. [28] Despite the continuous progress of the electrocatalysts for the production of H_2O_2, most of them solely function in a single electrolyte. Although a rapidly increasing body of research has been devoted to the electrocatalysis of H_2O_2, the wider pH approach is still very limited yet. It is highly desirable yet challenging to explore robust catalysts that work under pH conditions.

Compared to the metal alloys, the selection of noble metal-based chalcogenide shows advantages of the high abundance, low cost, and equivalent catalytic activity, indicating their high possibility in future applications for H_2O_2 production. In particular, the semi-metal nature of Se shows higher electroactivity than S, indicating the untapped potential in H_2O_2 production. Herein, we report a facile wet-chemical approach to synthesize highly monodisperse Pd_4Se nanoparticles (NPs), which is innovatively adopted for use as efficient electrocatalysts for highly selective H_2O_2 generation under pH-universal conditions. Compared to the commercial Pd/C and Pd NPs catalysts, Pd_4Se NPs exhibit a significant increase in oxygen reduction selectivity towards H_2O_2 production of 93.5%, 89.7%, and 86.7% between 0.2 and 0.45 V (vs. RHE) in 0.1 M $HClO_4$, in 0.1 M KCl and 0.1 M KOH electrolytes, respectively. The H_2O_2 generated among the chronoamperometric confirmed the excellent H_2O_2 productivity in the different electrolytes. While the superior activity for H_2O_2 production at pH-universal conditions is ascribed to the high electron density of the isolated Pd atoms, the Se atoms at the surface of the NPs are believed to influence the properties of Pd, resulting in the enhanced selectivity of the Pd_4Se NPs. DFT calculations reveal that Se-incorporation correlates with strong *p-d* repulsion that shifts the Pd-4d band towards the electron-depleting centre, enabling near-barrier-free electron transfer and facilitating [OOH^-] stabilization. The surface-engineered Pd substantially suppresses the HER and optimally mismatches the (O═O)− 2p band to allow for excellent serial protonation, which collectively results in efficient H_2O_2 synthesis. The Pd_4Se NPs also show excellent durability with limited H_2O_2 selectivity decreases in 0.1 M $HClO_4$, 0.1 M KCl and 0.1 M KOH electrolytes after 5000 cycles.

2. Results and discussion

2.1. Crystal structure of Pd_4Se NPs

The $2e^-$ reduction reaction only involves two single-proton-coupled electron transfers ($O_2 + * + H^+ + e^- \rightarrow OOH^*$, $OOH^* + H^+ + e^- \rightarrow H_2O_2 + *$) and generates an HOO* intermediate during the ORR process. Thus, if it ensured that OOH* is the only intermediate then H_2O_2 is selectively formed. Hence, the selectivity and activity of the catalyst not only depend on the binding energy of reaction intermediates but are also determined by the binding behaviour that is affected by the electronic structures of the catalyst. Recent theoretical studies have noted that the selectivity of H_2O_2 generation can be determined by adsorbing O_2 directly onto the surface of the isolated active metal during the ORR process. As shown in Fig. 1a, Pd_4Se NPs crystallizes in a tetragonal symmetry with the space group *P-421c* (114). The projected unit cell is composed of a periodic square array of pure Se columns surrounded by Pd columns at the corners of each unit cell. Correspondingly, there are two non-equivalent Se-Pd metallic bonds in the periodic square array, characterized by a slightly shorter Se-Pd distance (2.497 Å) and longer Se-Pd distance (2.539 Å) (Fig. 1b). As shown in Fig. 1c, the X-ray diffraction (XRD) pattern is consistent with the simulated pattern of single-crystal Pd_4Se. The Raman spectrum of Pd_4Se is presented in Fig. 1d, and the spectrum reveals bands at 136, 168, 232 and 271 cm^{-1}, which correspond to Pd_4Se. [29] Thus, this arrangement is conducive to the "end-on" adsorption of O_2, thereby increasing the selectivity of H_2O_2 production. In contrast, due to the presence of adjacent Pd-Pd metallic bonds in the unit cell (Fig. 1e,f), O_2 adsorption is mainly "side-on" rather than "end-on" on the surface of metals with adjacent active sites, thus reducing the selectivity of H_2O_2 production, being consistent with direct synthesis energy evolution on Pd NPs (Supplementary Figure 1–5 and Table 1).

2.2. Synthesis and characterization of the Pd_4Se NPs

The promising Pd_4Se NPs were synthesized by the simultaneous reduction of palladium(II) bromide ($PdBr_2$) and dibenzyl diselenide ($C_{14}H_{14}Se_2$) by using oleylamine as both the solvent and surfactant and ascorbic acid (AA) as the reducing agent (see more details in the Experimental Section). It is significant to screen the kinds of Pd-precursor for the fine control of Pd_4Se NPs. In comparison, using other Pd-precursors only results in the products with irregular shape and uniformity (Supplementary Figure 6). Fig. 1**g** and Supplementary Figure 7a show high-angle annular dark-field scanning transmission electron microscopy (HAADF-STEM) and TEM images of the obtained Pd_4Se NPs. According to Supplementary Figure 7, the products are composed of uniform spherical NPs, where the nanoparticles are uniformly monodispersed with an average size of 8.5 nm. The Pd/Se composition is 64.3/35.7, as determined by scanning electron microscopy energy-dispersive X-ray spectroscopy (SEM-EDS, Supplementary Figure 7), which is in accordance with the inductively coupled plasma atomic emission spectroscopy (ICP-AES) results. The X-ray diffraction pattern of the Pd_4Se NPs (Fig. 1**c**) possesses diffraction peaks at 31.7, 37.9, 40.2, and 41.8°, which are indexed to the (002), (201), (112), and (211) diffractions of face-centered cubic (*fcc*) Pd_4Se (JCPDS number 11–0498). As shown by the HRTEM image in Fig. 1**h**, the Pd_4Se NPs exhibit a high degree of crystallinity with a lattice spacing measured to be 0.185 nm, which is in accordance with the value of the (220) plane of Pd_4Se. The alloyed feature of the structure was further evidenced by HAADF-STEM elemental mapping analysis (Fig. 1**i**) and STEM-EELS line scans (Supplementary Figure 7), where Pd and Se are seen to be distributed evenly throughout the NPs.

2.3. X-ray absorption spectroscopy characterization of Pd_4Se NPs

To further verify the formation of isolated Pd atoms in Pd_4Se NPs/C, X-ray absorption spectroscopy (XAS) techniques were employed to evaluate the local coordination environment and chemical bonding of Pd4Se NPs/C. The Pd foil and commercial Pd/C were used as references. The Fourier transformation of the Pd K-edge EXAFS of Pd_4Se NPs is shown in Supplementary Figure 8a and further compared with that of Pd foil and commercial Pd/C. Specifically, the peak in the commercial Pd/C and Pd foil located at 2.52 Å, indicating the presence of the Pd-Pd bond. An obvious transition in the first shell bond length from 2.52 Å to 2.12 Å indicates that the adjacent Pd-Pd bond is not formed in Pd_4Se NPs/C (Supplementary Figure 8b). In addition, the formation of atomically dispersed Pd was further confirmed by the EXAFS wavelet transform (WT) analysis. According to the Supplementary Figure 8c-**d**, the WT analysis of Pd_4Se NPs/C indicates that there is only one intensity maximum locating at approximately 8.7 $Å^{-1}$, which is attributed to the

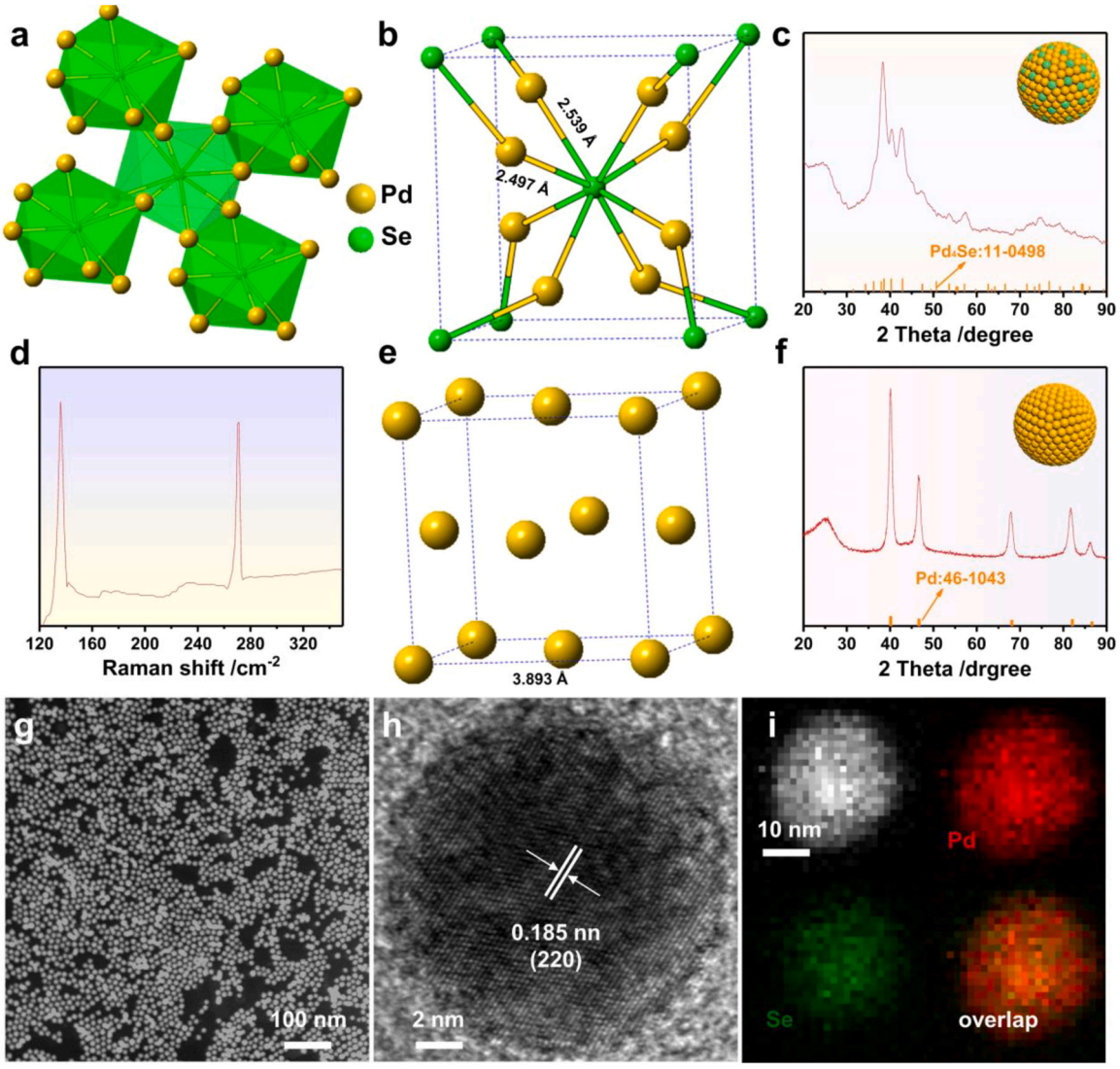

Fig. 1. Structural characterization of Pd_4Se NPs and Pd NPs. (a) Crystal structure, (b) local ball-and-stick model, (c) XRD pattern (inset is the corresponding geometric model for an individual Pd_4Se NP), and (d) Raman spectrum of Pd_4Se NPs. (e) Local *fcc*-Pd model and (f) XRD pattern (inset is corresponding geometric model for an individual Pd NP) of the Pd NPs. (g) HAADF-STEM image, (**h**) HRTEM image, and (**i**) HAADF-STEM image and elemental mapping of the Pd_4Se NPs.

coordination of Pd-Se. In contrast, the intensity maximum of Pd foil exhibits a larger positive shift to 10.5 $Å^{-1}$ due to the contribution from the longer Pd-Pd distances. The above results give solid evidence for the existence of the isolated Pd atoms in Pd_4Se NPs/C.

2.4. Electrochemical performance toward H_2O_2 synthesis of the different catalysts

The electrocatalytic performance of the obtained catalysts towards the ORR was evaluated using the rotating ring-disk electrode (RRDE) method. In order to conduct the electrocatalytic studies, the Pd_4Se NPs were deposited onto carbon support (C, Vulcan) and then annealed at 250 °C under H_2 (see more details in the Experimental Section). Such treatment endows the Pd_4Se NPs to be distributed uniformly onto the carbon support without essentially size or compositional changes as well as guaranteed the removal of surface capping agents. (Supplementary Figure 9 & Supplementary Figure 19). The ORR activity of the Pd_4Se NPs was evaluated by RRDE measurements in 0.1 M $HClO_4$. Fig. 2a,b show the measured oxygen reduction reaction currents and H_2O_2 oxidation currents at disk electrode (solid lines) and Pt ring electrode (dashed lines) in 0.1 M $HClO_4$ electrolyte. The rotating ring-disk electrode was employed to quantify the amount of H_2O_2 generated in which the ring electrode was fixed at 1.2 V (vs. RHE) to oxidize the H_2O_2 generated on the disk electrode. It can be observed from the polarization curves that the Pd_4Se NPs exhibit a noticeable higher current density and significantly lower overpotential (~53 mV lower at 1 mA cm^{-2}) compared to those of Pd NPs, indicating that the Pd_4Se NPs exhibit a higher activity for H_2O_2 production. In addition to the high selectivity of Pd_4Se NPs, they also exhibit a remarkably higher H_2O_2 selectivity, where the Pd_4Se NPs produce H_2O_2 with 93.5% selectivity, while the Pd NPs show a low H_2O_2 generation selectivity of 39.5% (Fig. 2c). This indicates that Pd_4Se NPs catalyse the ORR predominately through a $2e^-$ process (n = 2.2), whereas Pd NPs (n = 3.2) enables a mixture of the $2e^-$ and $4e^-$ pathways (Fig. 2d), successfully confirming the concept of using the O_2 adsorption mode to adjust the activity and selectivity of a catalyst toward ORR.

2.5. Electrochemical selectivity, potential production, and durability of Pd_4Se NPs for H_2O_2 synthesis under different pH conditions

The electrocatalytic performance of the obtained Pd_4Se NPs in various pH environments was then explored. In an acidic environment, the Pd_4Se NPs exhibit the highest selectivity, whereas a high selectivity is also obtained in an alkaline solution and a neutral solution. To understand the surface properties and determine the electrochemical

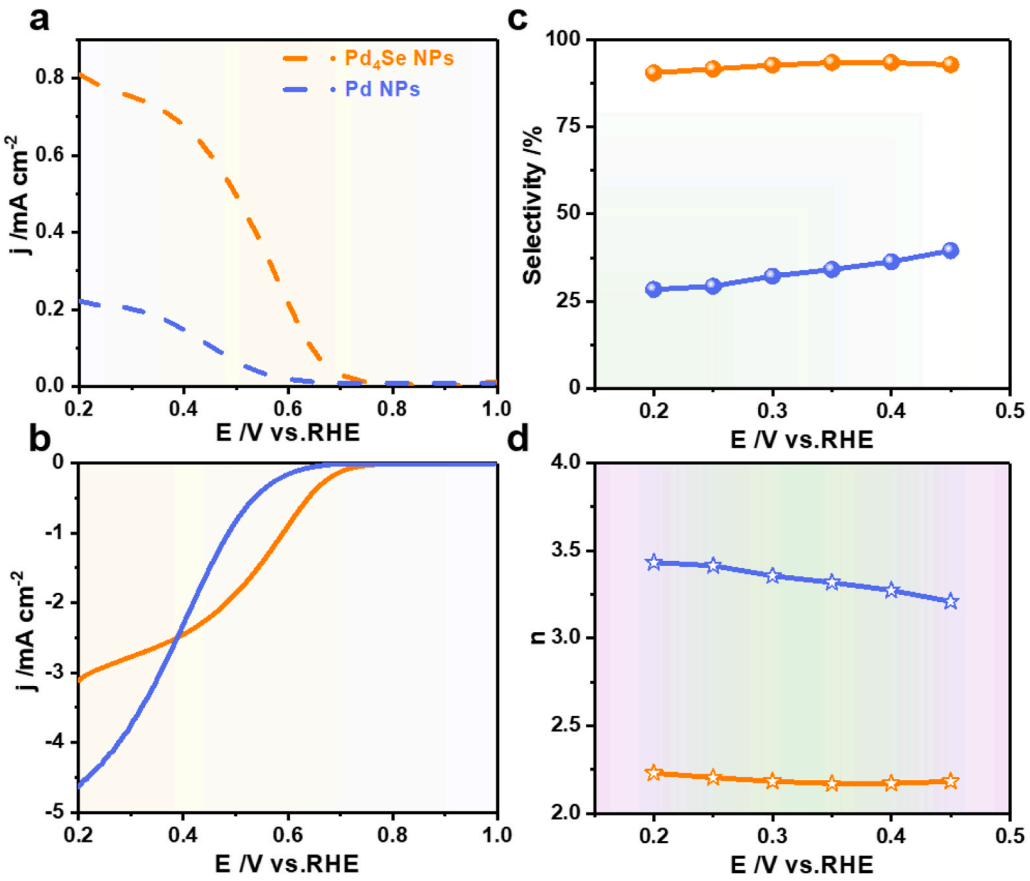

Fig. 2. Electrocatalytic properties for the synthesis of H_2O_2 on different catalysts. H_2O_2 detection currents at the (a) ring electrode (dashed lines) and polarization curves at the (b) disk electrode (solid lines) for the different catalysts in a 0.1 M $HClO_4$ electrolyte. Calculated (c) selectivities and (d) number of transferred electrons for the different catalysts at different potentials in a 0.1 M $HClO_4$. The colour scheme in (a) applies to (b-d).

surface areas (ECSA) of the catalyst, CO stripping experiments were explored. As shown in Supplementary Figure 10**,** the anodic wave of Pd NPs/C (Supplementary Figure 11–12) and Pd_4Se NPs/C among the range of about − 0.2–0 V in the first cycle was attributed to the oxidation of CO adsorbed on Pd. Compared with Pd NPs/C, the smaller CO adsorption peak of Pd_4Se NPs/C indicates the presence of abundant Se atoms on the surface of Pd_4Se NPs/C. In addition, the CO adsorption peak position of Pd_4Se NPs/C (−0.10 V vs. SCE) appears at a higher potential than that of Pd NPs/C (−0.12 V vs. SCE), revealing the lower affinity for the *OH. The ECSA of the Pd_4Se NPs and Pd NPs were measured to be 24.6 and 51.2 $m^2\ g^{-1}$ based on the area of CO stripping. The significant increment of the electron density in each local Pd site caused by the electron transformation from Se to Pd clearly explains the reason that the fewer Pd sites in Pd_4Se exhibit higher electroactivity than the Pd NPs. Fig. 3a,d,g shows the electrochemical results of various catalysts in different electrolytes (0.1 M $HClO_4$, 0.1 M KCl and 0.1 M KOH). It is shown that the Pd_4Se NPs exhibit noticeable ring current densities in the different electrolytes compared to that of the Pd NPs and Pd/C (Supplementary Figure 13), indicating that more H_2O_2 was produced over the Pd_4Se NPs. In addition, to quantitatively compare the activities of the different catalysts, their selectivities and average electron transfer numbers (n) (Fig. 3b,c,e,f,h,i) were calculated at various potentials in the different electrolytes. In all cases, the Pd_4Se NPs exhibited the highest ORR selectivity among all the tested catalysts. Specifically, at 0.4 V (vs. RHE), the selectivities and electron transferred numbers of the Pd_4Se NPs are 93.5% (2.2), 89.7% (2.2), and 86.7% (2.3) in 0.1 M $HClO_4$, 0.1 M KCl, and 0.1 M KOH, respectively, while the Pd NPs and the commercial Pd/C show much lower selectivities and higher electron transfer numbers (Supplementary Table 2). Besides the high selectivity, Pd_4Se NPs/C exhibits the optimized mass activity of 21.5 $A\ g^{-1}_{Pd}$ at 0.65 V (vs. RHE) in 0.1 M $HClO_4$. In addition to common acidic conditions, the Pd_4Se NPs/C also exhibits superior ORR activity for H_2O_2 generation in neutral conditions (0.1 M KCl, 165.4 $A\ g^{-1}_{Pd}$ at 0.65 V vs. RHE) and alkaline conditions (0.1 M KOH, 183.6 $A\ g^{-1}_{Pd}$ at 0.65 V vs. RHE), which subverts the general viewpoint that precious metals based electrocatalysts solely function in the single electrolyte. Finally, although the reported carbon-based electrocatalysts display excellent activity for ORR to H_2O_2 in neutral and alkaline conditions, their performances in the acid condition still display the low H_2O_2 selectivity with the high over-potential. Therefore, Pd_4Se NPs/C achieves superior performance for ORR to H_2O_2 under pH-universal conditions, which exceeds most previously reported catalysts (Supplementary Table 3–6).

The H_2O_2 selectivity during the synthesis is also employed to evaluate the electrocatalytic performance of a catalyst, which needs to measure the potential production of H_2O_2 in the catalysis process. The amount of H_2O_2 generated in different electrolytes was detected by using electrochemical H-cells. Fig. 4**a** shows the productivity of Pd_4Se NPs in an O_2-saturated 0.1 M $HClO_4$ electrolyte, which is normalized over the reaction time and produced at various potentials ranging from 0.2 to 0.3 V (vs. RHE). According to the results, the H_2O_2 productivity increases with the applied potential becoming increasingly negative over the investigated potential range. Furthermore, the production rate of the catalyst increased linearly with the enhancement of time, demonstrating continuous and stable H_2O_2 production. This stability in H_2O_2 formation was further confirmed via the corresponding steady reduction current, which was measured over 2 h in a 0.1 M $HClO_4$ electrolyte (Supplementary Figure 14). Additionally, the corresponding H_2O_2 production rates were measured in 0.1 M KCl and 0.1 M KOH electrolytes. The production rate of H_2O_2 is significantly influenced by the pH in electrolytes (Fig. 4d,g & Supplementary Table 7). H_2O_2

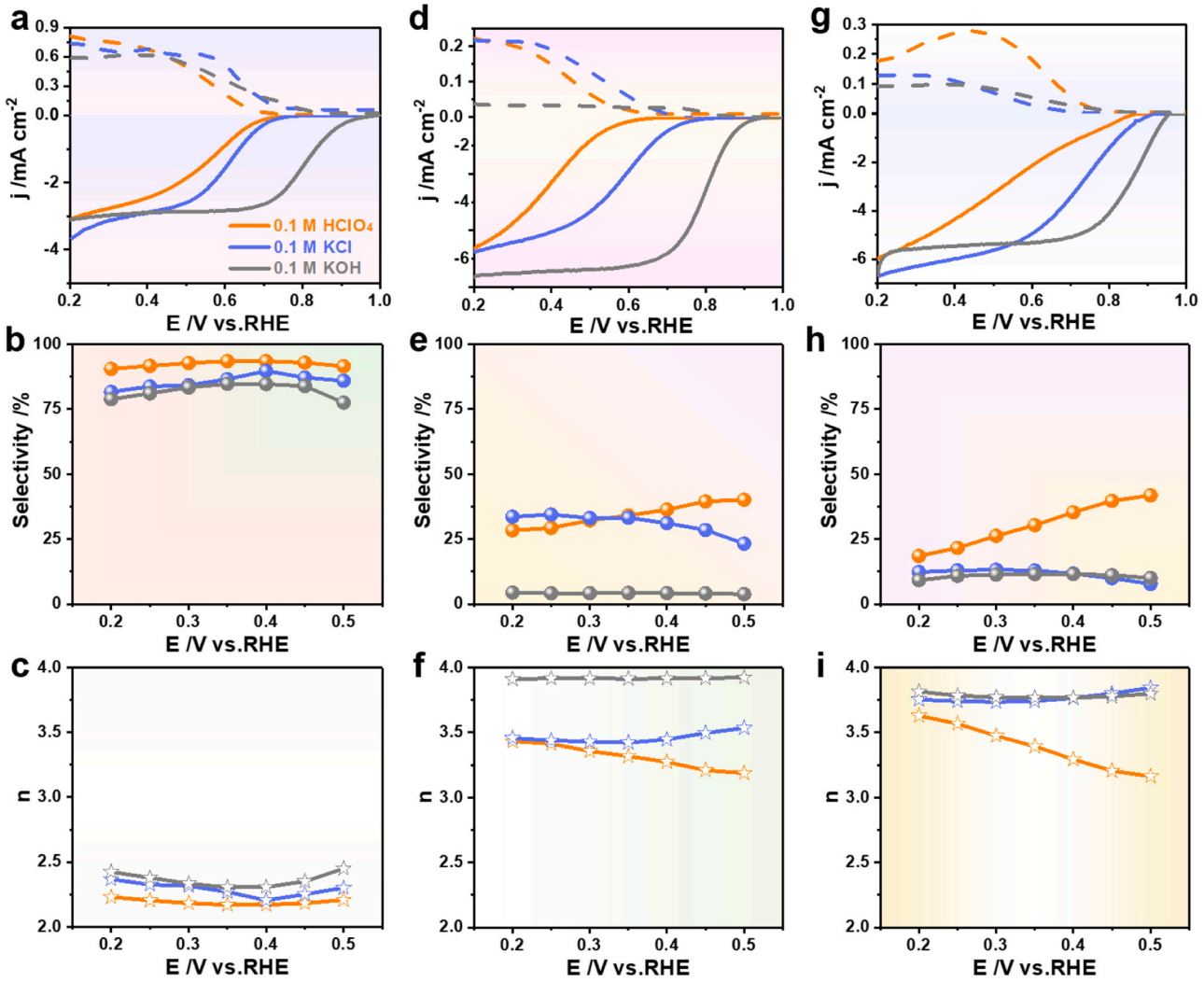

Fig. 3. Electrochemical measurements of the different catalysts for H_2O_2 synthesis in different electrolytes. Polarization curves at the disk electrode (solid lines) and simultaneous H_2O_2 detection currents at the ring electrode (dashed lines) for (a) Pd_4Se NPs, (d) Pd NPs and (g) Pd/C in different electrolytes. Calculated selectivities and number of transferred electrons of (b, c) Pd_4Se NPs, (e, f) Pd NPs and (h, i) Pd/C at various potentials in different electrolytes. The colour scheme in (a) applies to (b-i).

productivity of 9.31 mmol L^{-1} h^{-1} is obtained in 0.1 M KOH at 0.2 V (vs. RHE), which is 1.14 and 1.85 times higher than that in 0.1 M KCl and $HClO_4$ respectively, and is likely attributable to the different production mechanisms of H_2O_2 over Pd_4Se NPs in different electrolytes. The corresponding Faradaic efficiency of Pd_4Se NPs in the production electrolysis was also presented (Supplementary Figure 15). The electrolyte pH shows an impact on reactant (H_2O or H^+), the type of the peroxide species (HO_2^- or H_2O_2), and the consequent standard electrode potential of the reaction. The standard electrode potential in alkaline medium ($U_0^{O2/HO2-} = 0.76$ V vs. RHE, $O_2 + H_2O + 2e^- \rightarrow HO_2^- + OH^-$) is higher than that in acid medium ($U_0^{O2/H2O2} = 0.7$ V vs. RHE, $O_2 + 2e^- + 2H^+ \rightarrow H_2O_2$), indicating H_2O_2 is easier to form in alkaline electrolyte.

The ORR durability of the Pd_4Se NPs was evaluated. To this end, the ORR performance of the Pd_4Se NPs was studied before and after 5000 cycles stability test. According to Fig. 4b,e,h, the ORR polarization curves of the Pd_4Se NPs in different electrolytes exhibit minor changes even after 500 sweeping cycles. As shown in Fig. 4c,f,i and Supplementary Table 8, the Pd_4Se NPs show only 2.4%, 9.6% and 3.4% loss in the H_2O_2 production activity after the 5000-cycle durability tests in 0.1 M $HClO_4$, 0.1 M KCl and 0.1 M KOH electrolytes, respectively. Furthermore, the stability of electrocatalysts is evidenced by the Faradaic efficiency (Supplementary Figure 16). The electrocatalysts after the stability test were also characterized by HRTEM, TEM and SEM-EDS, where no obvious changes have been noted in the Pd_4Se NPs after 5000 cycles (Supplementary Figure 17–18). Therefore, the Pd_4Se NPs not only exhibit excellent H_2O_2 production activity but also superior durability.

2.6. *Surface characterization of the Pd_4Se NPs for H_2O_2 synthesis*

To understand the excellent activity and selectivity of Pd_4Se NPs toward H_2O_2 production, X-ray photoelectron spectroscopy (XPS) measurement was then performed to study the surface of the Pd_4Se NPs (Fig. 5a,b & Supplementary Figure 19). The Pd XPS of the Pd_4Se NPs exhibits peaks of $3d_{5/2}$ and $3d_{3/2}$, which could be split into doublets related to Pd^0 and Pd^{2+}, respectively. The peaks at the B.E. of 54.3 and 54.9 eV are ascribed to the orbitals of Se $3d_{5/2}$ and $3d_{3/2}$, which are referred to the oxidation state of − 2 for Se_2 (Se_2^{2-}). An additional peak located at 58.3 eV suggests a Se species in an oxide state (SeO_x) (Supplementary Figure 19). [30–34] Compared to the B.E. of Pd^0 in Pd NPs (336.1 eV), the lower BE of Pd^0 in the Pd_4Se NPs (335.9 eV) indicates a higher electron density on Pd, mainly caused by the electron transformation from Se to Pd. The higher electron density of the surface-residing Pd in the Pd_4Se NPs benefits the adsorption of OOH*,

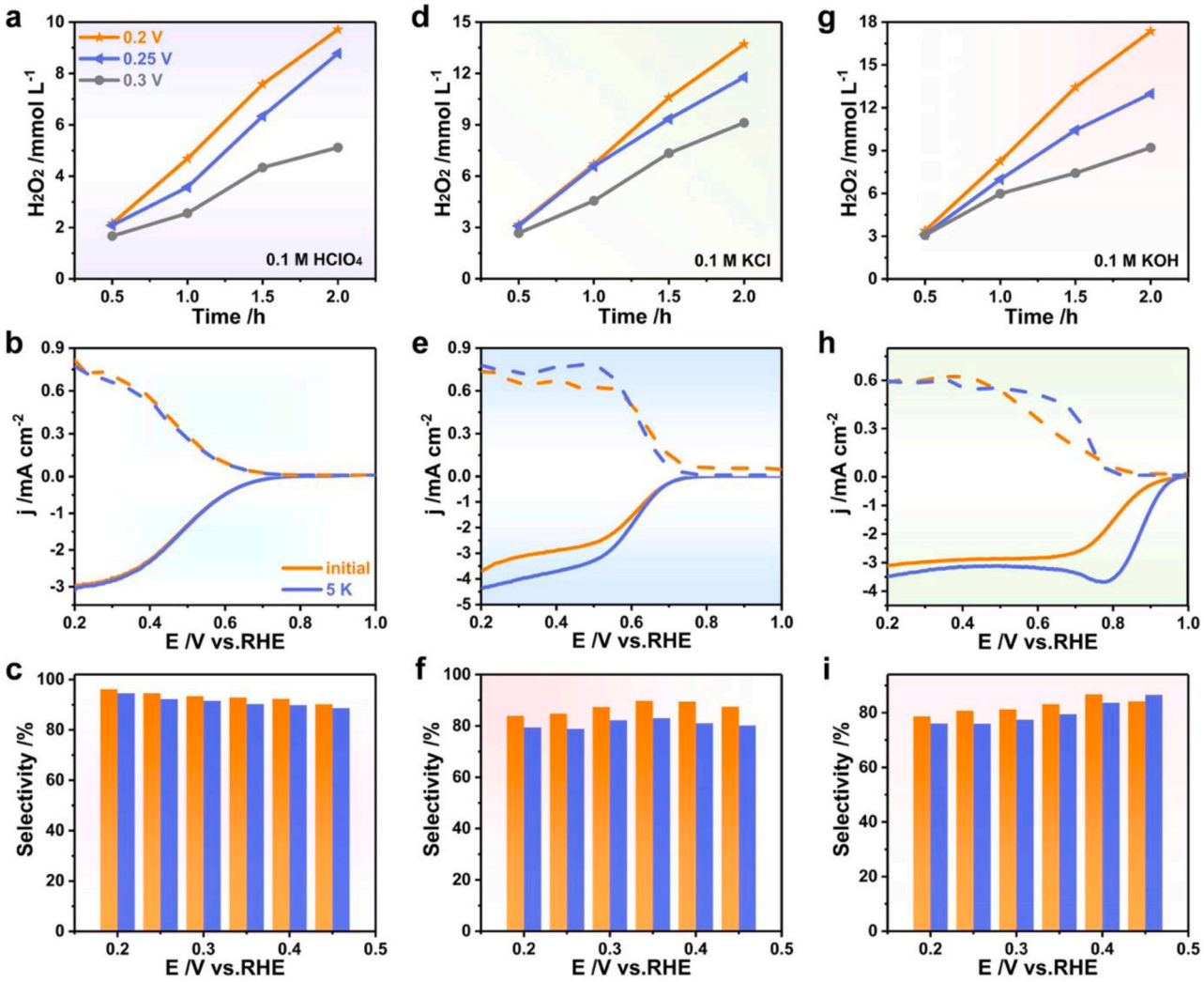

Fig. 4. Electrochemical potential production and durability of Pd_4Se NPs for H_2O_2 synthesis. H_2O_2 production over the reaction time at various potentials of Pd_4Se NPs in O_2-saturated (a) 0.1 M $HClO_4$, (d) 0.1 M KCl and (g) 0.1 M KOH. Polarization curves at the disk electrode (solid lines) and simultaneous H_2O_2 detection currents at the ring electrode (dashed lines) and calculated selectivity for Pd_4Se NPs at various potentials in (b, c) 0.1 M $HClO_4$, (e, f) 0.1 M KCl and (**h, i**) 0.1 M KOH before (orange) and after (blue) durability tests.

which is also confirmed by the surface valence band photoemission spectra (Fig. 5b). [35–37] In general, both $2e^-$ ORR to H_2O_2 and $4e^-$ ORR to H_2O start with the formation of OOH* via the reduction of O_2* and H^+ ($O_2^* + e^- + H^+ \rightarrow OOH^*$), which means that the stronger adsorbed OOH* species benefit to H_2O_2 production as well as $4e^-$ ORR to H_2O. Subsequently, the selectivity of H_2O_2 is determined whether OOH* is further reduced to HOOH* ($OOH^* + e^- + H^+ \rightarrow HOOH^*$) or dissociates to OH* and O* ($OOH^* + * \rightarrow OH^* + O^*$). Based on the result of structural analysis (Supplementary Figure 8) and performance tests (Fig. 3), we conclude the proposed reaction pathway for O_2 reduction on the catalytic surface of the Pd NPs and Pd_4Se NPs (Fig. 5c). For Pd NPs, the side-on mode is energetically favorable than the end-on mode due to the presence of adjacent Pd sites, thus, OOH* adsorption mainly follows the mode of "side-on" rather than the "end-on" adsorption. In detail, the "side-on" adsorption mode of O_2 weakens the O-O bond, thereby inducing the $4e^-$ process, which involves the O-O dissociation (Fig. 5c, left). In contrast, the O_2 will absorb on the surface in end-on mode at the presence of isolated Pd atoms and both H_2O and H_2O_2 are the final products via competitive $4e^-$ (dissociation of O-O bond) or $2e^-$ (desorption of *OOH) pathways, respectively (Supplementary Figure 8). [14] Additionally, the presence of Se atoms on the surface of Pd_4Se NPs separates the continuous Pd atoms to form the active isolated Pd sites. The monatomic Pd sites suppress the dissociation of OOH* to O* and OH* and thus increases the selectivity of H_2O_2 production (Fig. 5c, right).

2.7. Theoretical investigation

To understand the enhancement of performance observed in the experiments, we characterize the excellent performance for H_2O_2 synthesis with DFT calculations. The bonding and anti-bonding orbitals near the Fermi level (E_F) demonstrate different surface electronic density distributions brought about by adsorption, which further modulates the electroactivity. (Fig. 6a). The site-dependent electroactivity trend of the Pd-4d band was identified from the projected partial density of states (PDOSs). The centre of the Pd-4d band shifts towards E_V-2.2 eV, which is higher than that of the original Pd-fcc (E_V-2.6 eV, $E_V = 0$ for E_F), supporting a smaller barrier for electron transfer. From the deep bulk (Pd-db) to near-surface (Pd-ns) and surface (Pd-s) regions, the Pd-4d band monotonically shifts upwards towards E_V-1.5 eV near E_F, which indicates an electron-depleting role allowing for better electron transfer to the O/H-species (Fig. 6b). The interplay of the Pd-4d and Se-4p orbitals has been illustrated. A strong *p-d* coupling between the Pd-4d and Se-4p sites leads to variations in the behaviours of the local electronic

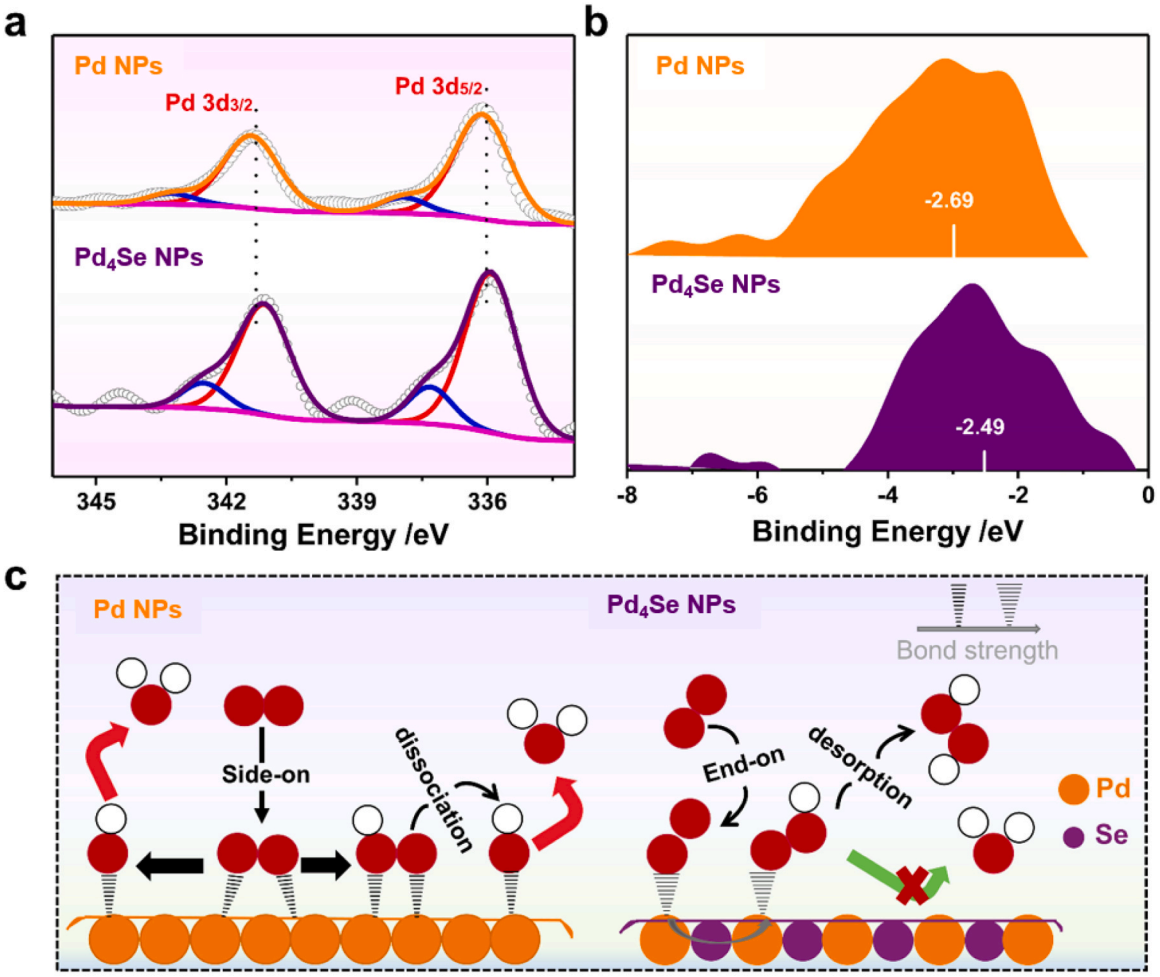

Fig. 5. Surface characterization of the Pd_4Se NPs and proposed mechanism for H_2O_2 synthesis. (a) XPS patterns of Pd 3d from the Pd NPs and Pd_4Se NPs and (b) surface valence band photoemission spectra. (c) Schematic showing the proposed mechanism for O_2 reduction on the catalytic surface of the Pd NPs (left) and Pd_4Se NPs (right). Red is O and white is H. The relative intermediate binding strength is indicated by the hashed wedged bond (in the top right corner).

environment. PDOSs analysis shows that the Se-4p and Pd-4d bands are both sensitive to changes in the different bonding environments and the lattice relaxation. Such a trend crucially facilitates the stabilization of [OOH^-] species and their subsequent protonation into H_2O_2 (Fig. 6c). We further demonstrate the individual contributions of the 1 s/2p-bands from the H/O-related species during H_2O_2 catalysis. The difference of O-2p bands between the free and adsorbed O_2- indicates that electron transfer from the O-2pπ lone-pair towards the deep-lying O-2pσ band. The relative position of the O═O 2p state to that of the modified Pd-4d band is key to the optimal preservation of [OOH^-] without an early scissoring effect (Fig. 6d).

We further illustrate the unique role of the surface Pd sites. For O_2 adsorption, the Pd-4d band evidently downshifts to a lower position, becoming more electron-rich. This characteristic is an essential step necessary for preventing an excessive electron population on the *O═O molecules, leading to the potential O═O bond cleavage by strong pπ-pπ Coulombic repulsion (Fig. 6e). For stabilizing [OOH^-], PDOSs analysis confirms that the Pd-4d band efficiently transfers electrons between adsorbed *O═O and 2 H* , assisted by the upshifting of the Pd-4d band from E_V-2.6 eV to E_V-1.5 eV in the case of [OOH]-adsorption (Fig. 6f). We further compared the Pd-4d band centres for the different cases of H_2O_2 formation and other intermediates that deviate from the synthetic route for H_2O_2. The high-lying Pd-4d band facilitates H-adsorption and electron transfer between the H and O species via the Pd-4d orbital. The modified Pd-4d band plays a facilitating role in electronically stabilizing the [OOH^-] for secondary protonation (Fig. 6g).

Theoretical calculations further confirm the preference of end-on mode on the SePd surface than the Pd NPs regarding both adsorption energies and structural configurations. In addition, the much stronger adsorption strength of *OOH is noted on both Pd surfaces and nanoparticle structures. Both conditions result in the further dissociation of O-O bond, which significantly lowers the selectivity towards H_2O_2 (Supplementary Figure 20). The synthesis approach under different environments has been considered. For the acidic environment, the continuous pathway with each step scale around 0.71 eV has been identified, which is close to the equilibrium potential of 0.7 V under the acidic environment. This indicates a low overpotential based on the efficient electron transfer for generating H_2O_2. The competing four-electron pathway has also been demonstrated to reveal the origins of high selectivity for SePd electrocatalyst, in which the electrochemical barriers determine the selectivity. Notably, the formation of H_2O_2 * (0.14 eV) shows a much smaller energy barrier than the dissociation of *OOH (0.55 eV), which guarantees the high selectivity of H_2O_2 generation (Fig. 7a & Supplementary Figure 21). Meanwhile, for the base/alkaline environment, the equilibrium potential slightly increases. As a consequence, the two charge-transfer steps show the reaction free energies of the same magnitude equal to the equilibrium potential of 0.76 eV/electron transfer, also supporting the remarkable performance of H_2O_2 production. Although the generation of water is thermodynamically favorable, the large barrier of 0.44 eV for *OOH dissociation to *O and *OH leads to the dominating 2-electron pathway to the generation of H_2O_2 (Fig. 7b & Supplementary Figure 21). Beyond the typical

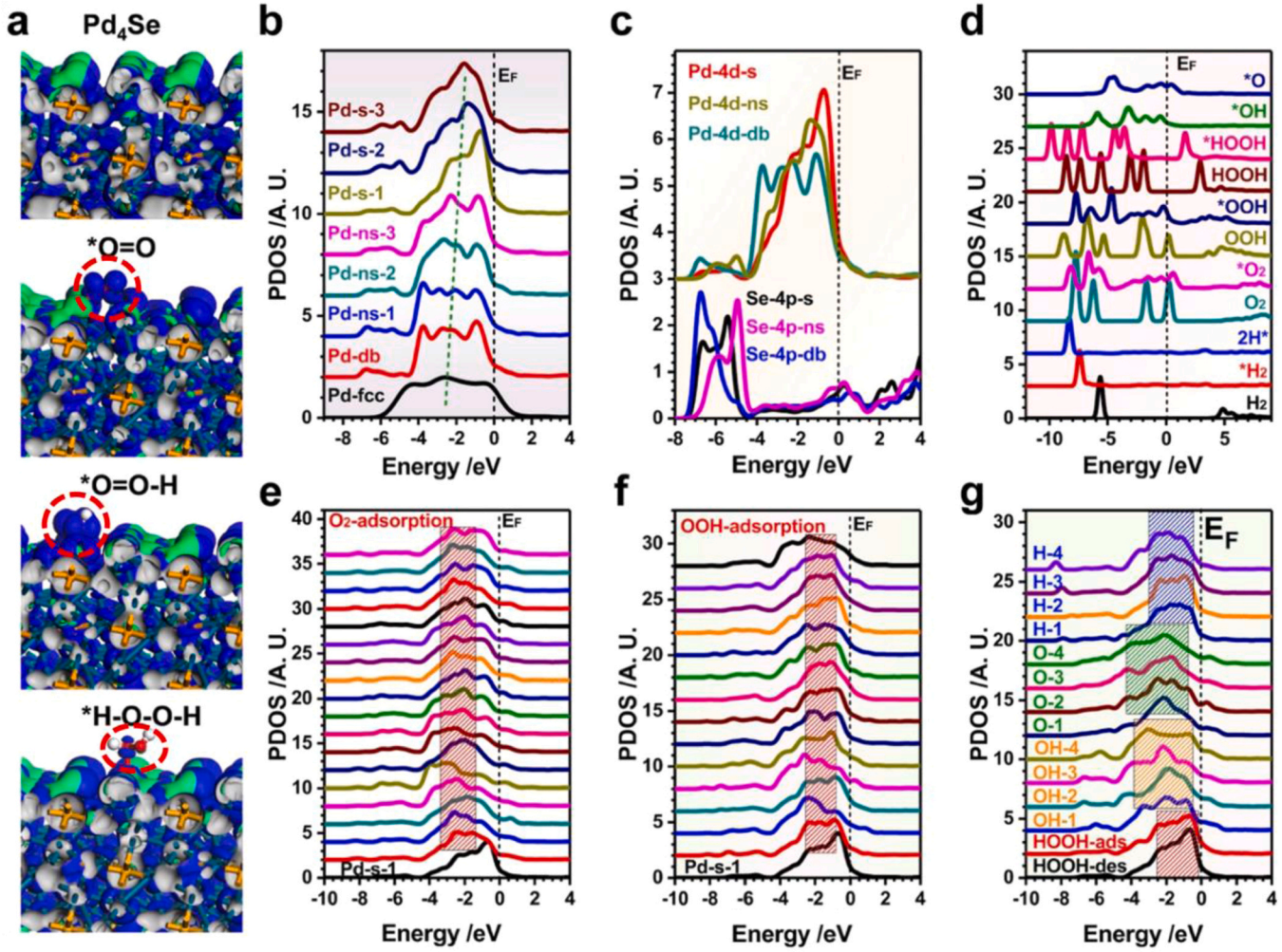

Fig. 6. Electronic structures and activities of SePd for the synthesis of H_2O_2. (a) The real spatial contour plots for the bonding and anti-bonding orbitals near E_F of SePd with different adsorbed H/O species. (b) Variations in the PDOSs behaviour of the site-dependent 4d-band of the Pd-sites within the SePd system with reference to the Pd-fcc bulk state (where s = surface, ns = near-surface, and db = deep bulk regions of SePd). (c) Site-dependent PDOSs correlations between the Se-4p and Pd-4d bands. (d) PDOSs for different s/p-band ranges of the various H/O species. (e) PDOSs of the different structural configurations of O_2 adsorbed onto SePd. (f) PDOSs of the different structural configurations of OOH adsorbed onto SePd. (g) Variation trends for the PDOSs of the Pd-4d band for the successful formation of H_2O_2 compared with those of the H/O intermediates, which deviate from the synthetic route.

electrocatalyst, we also considered the direct synthesis of H_2O_2 (DSHP), which shows a more complex mechanism. Regarding the direct protonation of [OOH^-], the formation of H_2O_2 is shown to be energetically favorable (−0.97 eV), and the related desorption step has an energy barrier of only 0.22 eV. In comparison, such direct protonation has been significantly suppressed on the Pd NPs due to the intensive energy barrier of 1.54 eV. The consecutive desorption also requires 0.73 eV, indicating the low selectivity of H_2O_2 on Pd NPs. The initial adsorption of O_2 and 2 H on Pd_4Se gains − 0.52 eV of energy compared to the free molecular state. We notice that the process for forming [OOH^-] has a barrier of 0.25 eV in the primary protonation step, which is also denoted as the potential determining step (PDS). This barrier height is close to the desorption energy of H_2O_2, resulting in a catalytic performance with a substantially high rate (Fig. 7c). The energetic gain indicates that the local active sites substantially promote the Se-Pd transfer and inhibit the O-O bond cleavage through the energetic competition. Detailed binding energies comparisons support weak desorption of OOH and weak adsorption of [HOOH] guarantee the stable protonation of [OOH^-] and efficient generation of H_2O_2 (Supplementary Figure 20). Further, the local structural configurations of *O═O and * [OOH^-] exhibit similar "end-on" structural configurations, which are advantageous for serial protonation and O-O cleavage suppression. This agrees with a consistent trend that the O-O bonding preservation among the Pd-sites and species is the crucial factor for excellently preserving [OOH^-] (Fig. 7d). Beyond the thermodynamic investigation of the reactions, we also interpret the kinetics simulations to demonstrate the dynamic behaviors of each step for the generation of H_2O_2 in Supplementary Information (Supplementary Figure 22–28, Table 9–15).

3. Conclusion

In conclusion, we first show that Pd_4Se NPs as efficient catalysts for electrochemical H_2O_2 production under pH-universal conditions. The Pd_4Se NPs exhibit superior H_2O_2 production selectivity of 93.5%, 89.7%, and 86.7% in 0.1 M $HClO_4$, 0.1 M KCl and 0.1 M KOH electrolytes, respectively. The remarkable activity of the Pd_4Se NPs is ascribed to the high electron density of the isolated Pd atoms owing to the electronic interaction between Se and Pd, and the superior selectivity is due to the existence of Se in Pd_4Se NPs, which passivates the isolated Pd atoms to prevent OOH* from being further reduced. The Pd_4Se NPs deliver stable and continuous H_2O_2 production at different applied potentials. DFT calculations reveal that the surface engineered Pd-sites, upon Se incorporation, optimally elevate the Pd-4d electron-transfer efficiency allowing for direct synthesis of H_2O_2 within self-locked-in

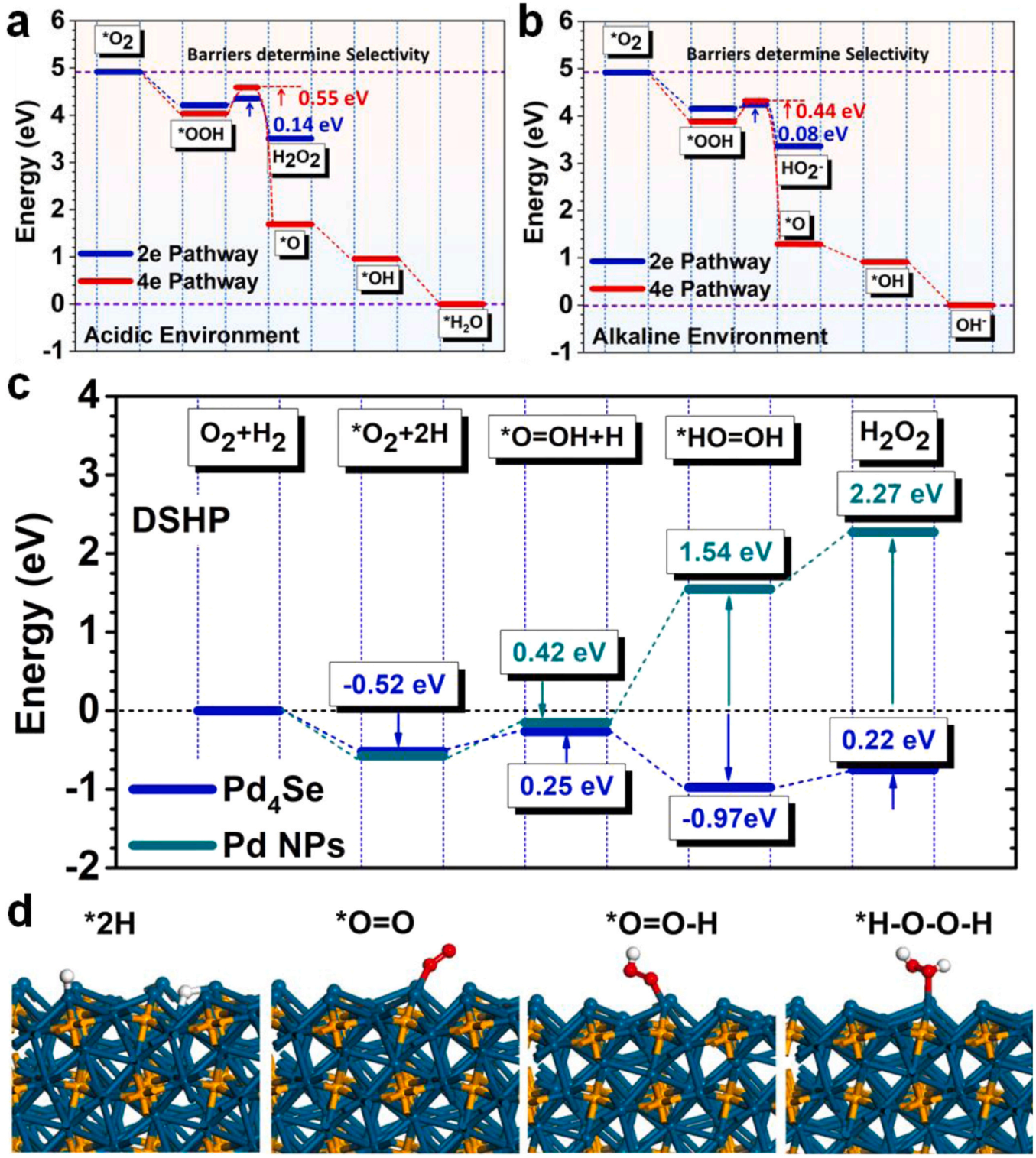

Fig. 7. H_2O_2 general energetic pathway in different environments. (a) Comparison of H_2O_2 synthetic pathway with 4-electrons pathway on the SePd under acidic environment. (b) Comparison of H_2O_2 synthetic pathway with 4-electrons pathway on the SePd under alkaline environment. (c) H_2O_2 synthetic pathway on SePd and Pd based on DSHP. (d) Structural configuration evolution of the synthesis of H_2O_2 during the catalytic process on SePd.

dynamics and suppression of four-electron pathway. A strong Coulombic repulsive correlation between the Se-4p_z and Pd-4d^{10}-t_{2g} states not only mismatches the O-2p band to excellently preserve side-on O═O adsorption but also facilitates [OOH^-] stabilization through efficient electron transfer, collectively resulting in optimal preservation of the O═O and [OOH^-] species for efficient H_2O_2 synthesis. Finally, the Pd_4Se NPs are very stable and largely maintain their performance, morphology and composition after 5000 cycles of a durability test, thus providing a new class of robust Pd-based nanocatalysts with high performance for electrochemical H_2O_2 production under pH-universal conditions.

3.1. Experimental section

3.1.1. Synthesis of Pd_4Se Nanoparticles (NPs)

In a typical synthesis of Pd_4Se NPs, 6.1 mg $PdBr_2$, 1.9 mg $C_{14}H_{14}Se_2$, 35.6 mg $C_6H_8O_6$ and 5 mL oleylamine (OAm) were added into a vial (volume: 30 mL). The mixture was ultrasonicated for around 0.5 h, after the vial had been capped. The obtained homogeneous mixture was then heated from room temperature to 160 °C for about 0.5 h and kept at 160 °C in an oil bath for 5 h. After cooling to room temperature, the colloidal product was washed 3 times with 0.5 mL cyclohexane and 8 mL ethanol, and collected by centrifugation at 12,000 rpm for 2 min

3.1.2. Preparation of supported catalysts

Pd_4Se NPs were mixed with VC-X72 carbon powder in 10 mL of cyclohexane and followed 0.5 h sonication to deposit Pd_4Se NPs onto C powder. The product was washed by centrifugation and sonication 3 times with cyclohexane and ethanol. The Pd_4Se NPs/C was then mixed with 0.5 mL acetic acid (HAc) and 5 mL ethanol followed by sonication with 10 min for further cleaned. The powder was finally washed with deionized water and annealed at 250 °C in a 5% H_2/95% N_2 atmosphere for 1 h.

3.1.3. Electrochemical Measurement

The oxygen reduction reaction (ORR) activities were performed using the rotating ring-disk electrode (RRDE) setup with a potentiostat in a three-electrode beaker cell. The three electrodes arrangement include saturated calomel electrode (SCE) as reference electrode, a platinum (Pt) wire as counter electrode, and a glassy carbon electrode consist of rotating disk electrode (RDE, 0.196 cm^2) and rotating ring-disk electrode (RRDE, 0.247 cm^2) measurement with a Pt ring. To prepare working electrode with the catalyst-coated, the catalysts were then dispersed in a mixture containing Nafion (5%) and isopropanol to form a 1.0 mg_{Pd}/mL dispersion. After sonication, the catalyst ink was dropped onto the newly polished glassy carbon electrode to obtain a working electrode after the solvent was naturally dried. All potentials are referred to the reversible hydrogen electrode (RHE).

ORR measurement was conducted in the aqueous solution of 0.1 M $HClO_4$, 0.1 M KCl, and 0.1 M KOH with O_2 purged during the measurement. The scan and rotation rate for ORR measurement were 10 mV s^{-1} and 1600 rpm, respectively. The ring currents were detected by fixing the ring potential at 1.2 V (vs. RHE) in order to collect the amounts of H_2O_2 produced on disk electrode. The stability tests were performed in the aqueous electrolyte (0.1 M $HClO_4$, 0.1 M KCl, and 0.1 M KOH) with the potential cycled between 0.4 and 0.8 V (vs. RHE) for 5000 cycles at 100 mV s^{-1}. After 5000 sweeping cycles, ORR measurement was performed in O_2-saturated solutions by applying the cyclic potential with O_2 purged during the measurement. The rotation rate and scan for ORR measurement were 1600 rpm and 10 mV s^{-1}, respectively. The collection efficiency (N = 29%) of the RRDE electrode was determined by using the reversible $[Fe(CN)_6]^{4-}/[Fe(CN)_6]^{3-}$ reaction. The selectivity of the electrocatalysts toward H_2O_2 generation was calculated by the following Eq. (1):

$$H_2O_2\% = 200 \times (I_R/N)/(I_R/N - |I_D|) \quad (1)$$

where I_D is the disk currents and I_R is the ring currents. The number of transferred electrons (n) during oxygen reduction reaction was calculated using the following Eq. (2):

$$n = 4 \times |I_D|/(I_R/N - I_D) \quad (2)$$

The Faradaic efficiency during the oxygen reduction process is defined as the following Eq. (3):

$$\text{Faradaic efficiency } (\%) = 100*(I_R/N)/|I_D| \quad (3)$$

The Faradaic efficiency of the generated H_2O_2 in the electrolysis can be calculated using formula (4):

$$H_2O_2 \text{ faradaic efficiency } (\%) = 2 \times F\ C\ V/Q \quad (4)$$

Where *F*, *C*, *V*, and *Q* represent the Faraday constant (96,485 C mol^{-1}), the H_2O_2 concentration (mmol L^{-1}), the volume of the electrolyte (L), and the amount of charge transferred in the process (C).

H_2O_2 concentration measurement. The H_2O_2 concentration was determined by a traditional cerium sulfate $Ce(SO_4)_2$ titration method according to the mechanism that the yellow solution of Ce^{4+} is reduced by H_2O_2 to colorless Ce^{3+} (Eq. (5)). Thus, the concentration of Ce^{4+} before and after the reaction is measured by UV-Vis spectroscopy. The wavelength used for the measurement was 316 nm.

$$H_2O_2 + 2Ce^{4+} \rightarrow 2Ce^{3+} + 2H^+ + O_2 \quad (5)$$

Therefore, the amount of H_2O_2 (*M*) evolved can be determined as twice the molar of Ce^{4+} consumed.

3.1.4. Computational details

We carried the DFT + U [37] calculations by CASTEP code. [38] The Hubbard-U parameter has been self-consistently determined for the pseudized Pd-4d by our linear response method for U determination. [39,40] The geometry optimization used the Broyden-Fletcher-Goldfarb-Shannon (BFGS) algorithm through all calculations. The PBE functional was chosen for PBE + U calculations with a plane-wave basis set cutoff energy of 750 eV. The ensemble DFT (EDFT) method [41] is used for improving convergence of transition metal based system. For the Pd_4Se-core model, the Pd_4Se (220) surface has been cleaved within the symmetry group of *P-421c*. The primitive cell lattice constants are a = b = 5.31 Å, and c = 5.79 Å. The supercell is chosen with 2 × 2 × 1 with 448 atoms and 4 layers thick. The vacuum thickness is fixed to be 15 Å, and we set full free relaxation of all layers. For the Monkhorst-Pack k-point sampling, the reciprocal space integration was performed using the mesh of 2 × 2 × 1 [42] with Gamma-center-off, which was self-consistently selected for total energy minimization. With these special *k*-points, the total energy is converged to less than 5.0 × 10^{-7} eV per atom. The Hellmann-Feynman forces on the atom were converged to less than 0.001 eV/Å.

The Pd, Se, O and H norm-conserving pseudopotentials are generated using the OPIUM code in the Kleinman-Bylander projector form, [43] and the non-linear partial core correction [44] and a scalar relativistic averaging scheme [45] are used to treat the (Pd, Se) spin-orbital coupling effect. We chose the (4*d*, 5*s*, 5*p*), (4*s*, 4*p*), (2*s*, 2*p*) and (1*s*) states as the valence states of Pd, Se, O, and H atoms respectively. The RRKJ method is chosen for the optimization of the pseudopotentials. [46] The Hubbard U parameter has been self-consistently determined based on our previous developed method. [47] For all of the electronic states calculations in Pd_4Se surface models, we use the self-consistent determination for the U correction on the localized 4d orbitals to correct the on-site Coulomb energy of the electron spurious self-energy. By that method, the Hubbard U parameters on the half-filled shell of $4d^{11}$ orbitals of Pd is self-consistently determined to be U_d = 9.69 eV, based on our devised linear response method. [47].

CRediT authorship contribution statement

X.H. and B.H. conceived and supervised the research. X.H., C.Y and S.B. designed the experiments. X.H., C.Y., S.B., Y.F., and T.Z. performed most of the experiments and data analysis. Z.Y. performs the additional experiments and data analysis during revisions. B.H. performed the theoretical computations and leading the theoretical exploration of in-depth mechanisms. M. S. and T. W. contributed to DFT calculations and discussions. Q. L. performed the kinetic simulations. C.C., L.Z. performed the X-ray absorption spectroscopy and analyzed the results. X.H., C.Y., S.B., Z.Y., Y.F., T.Z. and Q.S. participated in various aspects of the experiments and discussions. All authors contribute to the manuscript preparations. The authors would like to thank TLS (beamline

17C1) and TPS (beamline 44A) for the allocation of synchrotron beamtime C.

Declaration of Competing Interest

The authors declare that they have no known competing financial interests or personal relationships that could have appeared to influence the work reported in this paper.

Acknowledgements

The authors gratefully acknowledge the support of the Natural Science Foundation of China (Grant No.: NSFC 21771156).

Appendix A. Supporting information

Supplementary data associated with this article can be found in the online version at doi:10.1016/j.nanoen.2021.106480.

References

[1] K. Mase, M. Yoneda, Y. Yamada, S. Fukuzumi, Seawater usable for production and consumption of hydrogen peroxide as a solar fuel, Nat. Commun. 7 (2016) 11470.
[2] L. Han, S. Guo, P. Wang, S. Dong, Bending light via adiabatic optical transition in longitudinally modulated photonic lattices, Sci. Rep. 5 (2015) 15805.
[3] X. Shi, S. Siahrostami, G.L. Li, Y. Zhang, P. Chakthranont, F. Studt, T.F. Jaramillo, X. Zheng, J.K. Nørskov, Understanding activity trends in electrochemical water oxidation to form hydrogen peroxide, Nat. Commun. 8 (2017) 701.
[4] M. Melchionna, P. Fornasiero, M. Prato, The rise of hydrogen peroxide as the main product by metal-free catalysis in oxygen reductions, Adv. Mater. 31 (2019), 1802920, https://doi.org/10.1002/adma.201802920.
[5] N. Wilson, D. Flaherty, Mechanism for the direct synthesis of H_2O_2 on Pd clusters: heterolytic reaction pathways at the liquid-solid interface, J. Am. Chem. Soc. 138 (2016) 574–586.
[6] T.Murayama Yamanaka, Neutral H_2O_2 synthesis by electrolysis of water and O_2, Angew. Chem. Int. Ed. 120 (2008) 1926–1928.
[7] J.M. Campos-Martin, G. Blanco-Brieva, J.L. Fierro, Hydrogen peroxide synthesis: an outlook beyond the anthraquinone process, Angew. Chem. Int. Ed. 45 (2006) 6962–6984.
[8] S. Kanungo, V. Paunovic, J.C. Schouten, M.F. D'Angelo, Facile synthesis of catalytic AuPd nanoparticles within capillary microreactors using polyelectrolyte multilayers for the direct synthesis of H_2O_2, Nano Lett. 17 (2017) 6481–6486.
[9] S.J. Freakley, Q. He, J.H. Harrhy, L. Lu, D.A. Crole, D.J. Morgan, E.N. Ntainjua, J. K. Edwards, A.F. Carley, A.Y. Borisevich, C.J. Kiely, G.J. Hutchings, Palladium-tin catalysts for the direct synthesis of H_2O_2 with high selectivity, Science 351 (2016) 965–968.
[10] Y. Jiang, P. Ni, C. Chen, Y. Lu, P. Yang, B. Kong, A. Fisher, X. Wang, Selective electrochemical H_2O_2 production through two-electron oxygen electrochemistry, Adv. Energy Mater. 8 (2018), 1801909.
[11] Y. Sun, I. Sinev, W. Ju, A. Bergmann, S. Dresp, S. Kühl, C. Spöri, H. Schmies, H. Wang, D. Bernsmeier, B. Paul, R. Schmack, R. Kraehnert, B. Roldan Cuenya, P. Strasser, Efficient electrochemical hydrogen peroxide production from molecular oxygen on nitrogen-doped mesoporous carbon catalysts, ACS Catal. 8 (2018) 2844–2856.
[12] Katsounaros Cherevko S., A.R. Zeradjanin, K.J. Mayrhofer, Oxygen electrochemistry as a cornerstone for sustainable energy conversion, Angew. Chem. Int. Ed. 53 (2014) 102–121.
[13] R. Zhou, Y. Zheng, M. Jaroniec, S. Qiao, Determination of the electron transfer number for the oxygen reduction reaction: from theory to experiment, ACS Catal. 6 (2016) 4720–4728.
[14] S. Yang, A. Verdaguer-Casadevall, L. Arnarson, L. Silvioli, V. Čolić, R. Frydendal, J. Rossmeisl, I. Chorkendorff, I. Stephens, Toward the decentralized electrochemical production of H_2O_2: a focus on the catalysis, ACS Catal. 8 (2018) 4064–4081.
[15] S. Siahrostami, A. Verdaguer-Casadevall, M. Karamad, D. Deiana, P. Malacrida, B. Wickman, M. Escudero-Escribano, E.A. Paoli, R. Frydendal, T.W. Hansen, I. Chorkendorff, I.E. Stephens, J. Rossmeisl, Enabling direct H_2O_2 production through rational electrocatalyst design, Nat. Mat. 12 (2013) 1137–1143.
[16] J.S. Jirkovský, I. Panas, E. Ahlberg, M. Halasa, S. Romani, D.J. Schiffrin, Single atom hot-spots at au-pd nanoalloys for electrocatalytic H_2O_2 production, J. Am. Chem. Soc. 133 (2011) 19432–19441.
[17] A. Verdaguer-Casadevall, D. Deiana, M. Karamad, S. Siahrostami, P. Malacrida, T. W. Hansen, J. Rossmeisl, I. Chorkendorff, I.E. Stephens, Trends in the electrochemical synthesis of H_2O_2: enhancing activity and selectivity by electrocatalytic site engineering, Nano Lett. 14 (2014) 1603–1608.
[18] C. Xia, S. Back, S. Ringe, K. Jiang, F. Chen, X. Sun, S. Siahrostami, K. Chan, H. Wang, Confined local oxygen gas promotes electrochemical water oxidation to hydrogen peroxide, Nat. Catal. 3 (2020) 125–134, https://doi.org/10.1038/s41929-019-0402-8.
[19] Xia Xia Y., P. Zhu, L. Fan, H. Wang, Direct electrosynthesis of pure aqueous H_2O_2 solutions up to 20% by weight using a solid electrolyte, Science 366 (2019) 226–231.
[20] K. Jiang, S. Back, A.J. Akey, C. Xia, Y. Hu, W. Liang, D. Schaak, E. Stavitski, J. K. Nørskov, S. Siahrostami, H. Wang, Highly selective oxygen reduction to hydrogen peroxide on transition metal single atom coordination, Nat. Commun. 10 (2019) 3997.
[21] S. Chen, Z. Chen, S. Siahrostami, D. Higgins, D. Nordlund, D. Sokaras, T.R. Kim, Y. Liu, X. Yan, E. Nilsson, R. Sinclair, J.K. Nørskov, T.F. Jaramillo, Z. Bao, Designing boron nitride islands in carbon materials for efficient electrochemical synthesis of hydrogen peroxide, J. Am. Chem. Soc. 140 (2018) 7851–7859.
[22] R. Shen, W. Chen, Q. Peng, S. Lu, L. Zheng, X. Cao, Y. Wang, W. Zhu, J. Zhang, Z. Zhuang, C. Chen, D. Wang, Y. Li, High-concentration single atomic Pt Sites on Hollow CuS_x for selective O_2 reduction to H_2O_2 in acid solution, Chem 5 (2019) 2099–2110.
[23] Z. Zheng, Y.H. Ng, D. Wang, R. Amal, Epitaxial growth of Au-Pt-Ni nanorods for direct high selectivity H_2O_2 production, Adv. Mater. 28 (2016) 9949–9955.
[24] T.P. Fellinger, F. Hasché, P. Strasser, M. Antonietti, Mesoporous nitrogen-doped carbon for the electrocatalytic synthesis of hydrogen peroxide, J. Am. Chem. Soc. 134 (2012) 4072–4075.
[25] Q. Lu, X. Cai, X. Zhang, S. Li, Y. Song, D. Du, P. Dutta, Y. Lin, High-efficiency oxygen reduction to hydrogen peroxide catalysed by oxidized carbon materials, Nat. Catal. 1 (2018) 156–162.
[26] S. Yang, J. Kim, Y.J. Tak, A. Soon, H. Lee, Single-atom catalyst of platinum supported on titanium nitride for selective electrochemical reactions, Angew. Chem. Int. Ed. 55 (2016) 2058–2062.
[27] Y. Wang, G.I. Waterhouse, L. Shang, T. Zhang, Hollow CoP/FeP4 heterostructural nanorods interwoven by CNT as a highly efficient electrocatalyst for oxygen evolution reactions, Nanomater. (Basel) 11 (15) (2021), 2003323.
[28] Y. Jiang, P. Ni, C. Chen, Y. Lu, P. Yang, B. Kong, A. Fisher, X. Wang, Selective electrochemical H_2O_2 production through two-electron oxygen electrochemistry, Adv. Energy Mater. 8 (31) (2018), 1801909.
[29] S. Kukunuri, K. Naik, S. Sampath, Effects of composition and nanostructuring of palladium selenide phases, Pd_4Se, Pd_7Se_4 and $Pd_{17}Se_{15}$, on ORR activity and their use in Mg-air batteries, J. Mater. Chem. A 5 (2017) 4660–4670.
[30] B.J. Trześniewski, O. Diaz-Morales, D.A. Vermaas, A. Longo, W. Bras, M.T. Koper, W.A. Smith, In situ observation of active oxygen species in fe-containing ni-based oxygen evolution catalysts: the effect of pH on electrochemical activity, J. Am. Chem. Soc. 137 (2015) 15112–15121.
[31] B. Liu, Y.F. Zhao, H.Q. Peng, Z.Y. Zhang, C.K. Sit, M.F. Yuen, T.R. Zhang, C.S. Lee, W.J. Zhang, Nickel-cobalt diselenide 3D mesoporous nanosheet networks supported on ni foam: an all-pH highly efficient integrated electrocatalyst for hydrogen evolution, Adv. Mater. 29 (2017), 1606521.
[32] L.L. Feng, G. Yu, Y. Wu, G.D. Li, H. Li, Y. Sun, T. Asefa, W. Chen, X. Zou, High-index faceted Ni_3S_2 nanosheet arrays as highly active and ultrastable electrocatalysts for water splitting, J. Am. Chem. Soc. 137 (2015) 14023–14026.
[33] D. Kong, H. Wang, Z. Lu, Y. Cui, $CoSe_2$ Nanoparticles grown on carbon fiber paper: an efficient and stable electrocatalyst for hydrogen evolution reaction, J. Am. Chem. Soc. 136 (2014) 4897–4900.
[34] C. Tang, N. Cheng, Z. Pu, W. Xing, X. Sun, NiSe nanowire film supported on nickel foam: an efficient and stable 3D bifunctional electrode for full water splitting, Angew. Chem. Int. Ed. 127 (2015) 9483–9487.
[35] D. Kim, J. Resasco, Y. Yu, A.M. Asiri, P. Yang, Synergistic geometric and electronic effects for electrochemical reduction of carbon dioxide using gold-copper bimetallic nanoparticles, Nat. Commun. 5 (2014) 4948.
[36] H. Huang, H. Jia, Z. Liu, P. Gao, J. Zhao, Z. Luo, J. Yang, J. Zeng, Understanding of strain effects in the electrochemical reduction of CO_2: using Pd nanostructures as an ideal platform, Angew. Chem. Int. Ed. 129 (2017) 3648–3652.
[37] A. Vladimir, F. Aryasetiawan, A.I. Lichtenstein, First-principles calculations of the electronic structure and spectra of strongly correlated systems: the LDA + U method, J. Phys.: Condens. Matter 9 (1997) 767–808.
[38] S.J. Clark, M.D. Segall, C.J. Pickard, P.J. Hasnip, M. Probert, K. Refson, M. C. Payne, First principles methods using CASTEP, Z. Fur Krist. 220 (2005) 567–570.
[39] B. Huang, R. Gillen, J. Robertson, Study of CeO_2 and its native defects by density functional theory with repulsive potential, J. Phys. Chem. C. 118 (2014) 24248–24256.
[40] B. Huang, Unraveling energy conversion modeling in the intrinsic persistent upconverted luminescence of solids: a study of native point defects in antiferromagnetic Er_2O_3, Phys. Chem. Chem. Phys. 18 (2016) 13564–13582.
[41] N. Marzari, D. Vanderbilt, M.C. Payne, Ensemble density-functional theory for ab initio molecular dynamics of metals and finite-temperature insulators, Phys. Rev. Lett. 79 (1997) 1337–1340.
[42] M.I.J. Probert, M.C. Payne, Improving the convergence of defect calculations in supercells: an ab initio study of the neutral silicon vacancy, Phys. Rev. B 67 (2003), 075204.
[43] L. Kleinman, D.M. Bylander, Efficacious form for model pseudopotentials, Phys. Rev. Lett. 48 (1982) 1425–1428.
[44] S.G. Louie, S. Froyen, M.L. Cohen, Nonlinear ionic pseudopotentials in spin-density-functional calculations, Phys. Rev. B 26 (1982) 1738–1742.
[45] Grinberg Ramer N.J., A.M. Rappe, Transferable relativistic dirac-slater pseudopotentials, Phys. Rev. B 62 (2000) 2311–2314.
[46] A.M. Rappe, K.M. Rabe, E. Kaxiras, J.D. Joannopoulos, Optimized pseudopotentials, Phys. Rev. B Condens Matter 41 (1990) 1227–1230.

[47] B. Huang, The screened pseudo-charge repulsive potential in perturbed orbitals for band calculations by DFT + U, Phys. Chem. Chem. Phys. 19 (2017) 8008–8025.
[48] Xuan Zhao, Yanguang Li, Two-electron oxygen reduction reaction by high-loading molybdenum single-atom catalysts, Rare Metals 39 (2021) 455–457.
[49] Fuyan Xu, Tianshun Song, Yuan Xu, Yingwen Chen, Shemin Zhu, Shubao Shen, A new cathode using CeO_2/MWNT for hydrogen peroxide synthesis through a fuel cell, J. Rare Earths 27 (2009) 128–133.

Chengyong Yang is currently a postgraduate under the supervision of Prof. Xiaoqing Huang in College of Chemistry, Chemical Engineering and Materials Science in Soochow University. He received his B.S. degree in Huaiyin Normal University, China in 2017. His major is inorganic chemistry and he is now focusing on the design of noble metal nanomaterials for energy and environment applications.

Shuxing Bai is currently a Professor at College of Chemistry and Chemical Engineering, Qingdao University. He obtained his Ph.D. degree in industry catalysis from East China University of Science and Technology in 2016 under the supervision of Prof. Xingyi Wang. Then he continued his research as a postdoctoral in Prof. Xiaoqing Huang's group in College of Chemistry, Chemical Engineering and Materials Science in Soochow University. His current research interests are focusing on inorganic nanomaterials for energy and environmental catalysis.

Zhiyong Yu is currently a postgraduate under the supervision of Prof. Xiaoqing Huang in College of Chemistry, Chemical Engineering and Materials Science in Soochow University. He received his B.S. degree in Jiaxing University, China in 2019. His major is inorganic chemistry and he is now focusing on the design of noble metal nanomaterials for energy and environment applications.

Yonggang Feng is currently a Ph.D. candidate under the supervision of Prof. Huang in College of Chemistry, Chemical Engineering and Materials Science in Soochow University. He received his M.S degree in Soochow University, China in 2018 and B. S. degree in Jiaxing University, China in 2015. His major is inorganic chemistry and he is now focused on the design of noble metal nanomaterials for electrocatalysis and energy conversion.

Bolong Huang received his PhD in 2012 from the University of Cambridge, and his BSc in condensed matter physics from the Department of Physics, Peking University 2007. Following a systematic training period as a research assistant in the Chemistry Department at Peking University, and in Hong Kong, he was starting-up his independent research in the Hong Kong Polytechnic University in 2015 and become the Assistant Professor in 2017. His main research fields are electronic structures of nanomaterials, energy materials, solid functional materials, and rare earth materials, as well as their applications in multi-scale energy conversion and supply systems.

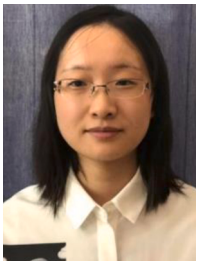

Qiuyang Lu born in 1991 in Jiangsu, China, studied biomedical engineering at Tianjin University (B.S. 2014) and received her master degree in the same subject from The Hong Kong Polytechnic University (M.S. 2017) on quantitative ultrasound with Dr. Lei Sun. Now she is a Ph.D. student of Dr. Bolong Huang at the Hong Kong Polytechnic University and her current research interest is on the image analysis about luminescence materials and electrification by Matlab simulations.

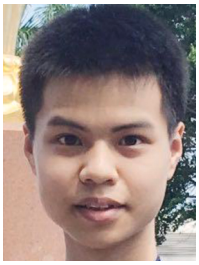

Tong Wu finished his bachelor's degree in the Hong Kong Polytechnic University in 2018 and has been working as a research assistant in Dr. Huang's group after graduation. He is now an PhD student and under the supervision of Dr. Huang and his current research interest is the advanced electrocatalysis with DFT calculations.

Mingzi Sun was born in Henan, China 1990. She studied chemistry at Sun-Yat Sen University (B.S. 2012) and received her master's degree in material science from the University of Rochester (M.S. 2014). She started working as an R&D engineer in a carbon nanotube production company for two years. She obtained PhD student under the supervision of Dr. Bolong Huang at the Hong Kong Polytechnic University at 2021. Her research interest is on the investigation of novel energy conversions of nanomaterials through DFT calculation methods.

Ting Zhu is currently a joint master student under the supervision of Professor Xiaoqing Huang in College of Chemistry, Chemical Engineering and Materials Science in Soochow University. He received his bachelor degree in Materials Chemistry from East China University of Technology in 2016. His research focuses on the design of metal-based nanomaterials for electrochemical water splitting.

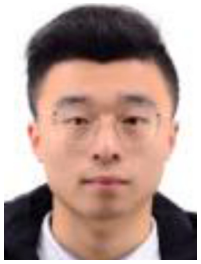

Chen Cheng received his bachelor degree from College of Environmental and Chemical Engineering of Shanghai University of Electric Power, July 2018. He is currently pursuing his Ph.D. degree under the supervision of Professor Liang Zhang at Soochow University, China. His research is mainly focused on the development and synchrotron characterization of cathode materials for sodium-ion batteries.

Liang Zhang is a Professor at Institute of Functional Nano & Soft Materials (FUNSOM), Soochow University, China. He received his Ph.D. from University of Science and Technology of China in 2013 and then worked as a postdoctoral fellow at University of Eralgen-Nuremberg, Germany and Lawrence Berkeley National Laboratory, United States. His current research focuses on the development and application of in-situ/operando synchrotron-based characterization techniques for energy storage materials.

Qi Shao received her Ph.D. degree in applied physics from City University of Hong Kong in 2016. Now she is an associate Professor in Professor Huang's group at College of Chemistry, Chemical Engineering and Materials Science, Soochow University. Her current research interests are focusing on non-noble metal-based catalysts for electrochemical applications.

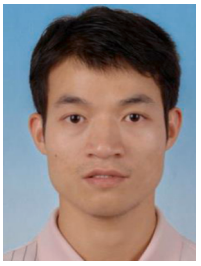

Xiaoqing Huang is currently a Professor at College of Chemistry and Chemical Engineering, Xiamen University. He obtained his B.Sc. in chemistry education from Southwest Normal University (2005) and Ph.D. in organic chemistry from Xiamen University (2011) under the supervision of Profs. Nanfeng Zheng and Lansun Zheng. Then he joined Profs. Yu Huang and Xiangfeng Duan's group as a postdoctoral research associate from September 2011 to June 2014 at University of California, Los Angeles. His current research interests are in the design of nanoscale materials for heterogenous catalysis, electrocatalysis, energy conversion and beyond.